

Adaptable GAN Encoders for Image Reconstruction via Multi-type Latent Vectors with Two-scale Attentions

Cheng Yu, Wenmin Wang, *Member, IEEE*

Abstract—Although current deep generative adversarial networks (GANs) could synthesize high-quality (HQ) images, discovering novel GAN encoders for image reconstruction is still favorable. When embedding images to latent space, existing GAN encoders work well for aligned images (such as the human face), but they do not adapt to more generalized GANs. To our knowledge, current state-of-the-art GAN encoders do not have a proper encoder to reconstruct high-fidelity images from most misaligned HQ synthesized images on different GANs. Their performances are limited, especially on non-aligned and real images. We propose a novel method (named MTV-TSA) to handle such problems. Creating multi-type latent vectors (MTV) from latent space and two-scale attentions (TSA) from images allows designing a set of encoders that can be adaptable to a variety of pre-trained GANs. We generalize two sets of loss functions to optimize the encoders. The designed encoders could make GANs reconstruct higher fidelity images from most synthesized HQ images. In addition, the proposed method can reconstruct real images well and process them based on learned attribute directions. The designed encoders have unified convolutional blocks and could match well in current GAN architectures (such as PGGAN, StyleGANs, and BigGAN) by fine-tuning the corresponding normalization layers and the last block. Such well-designed encoders can also be trained to converge more quickly.

Index Terms—Image reconstruction, Generative adversarial networks (GANs), GAN encoders, Multi-type latent vectors, Two-scale attentions.

I. INTRODUCTION

WITH the burgeoning development of deep generative adversarial networks (GANs) [2], [3], [4], [5], [6], high-quality (HQ) images can be generated with high resolutions of up to 1024×1024 pixels. The fundamental techniques include using the equalized learning rate to effectively and stably learn parameters in deeper networks, adding spectral normalization layers [7] or a gradient-penalty [8] on discriminators to satisfy the Lipschitz continuity, and increasing the training stability. Moreover, the mini-batch standard deviation

[9] could also be utilized in discriminators to increase the variety of outputs. The training methods for GANs have different variants, such as progressive training or using residual blocks [10]. Depending on these improvements, the effectiveness of GANs is sufficient for real image processing.

As an example of 1024×1024 HQ human face synthesis, there are often random and water-like droplets in synthesized images from PGGAN [4] and StyleGANv1 [1], and some image details always collapse when latent vectors deviate from the center. However, the upgraded model (StyleGANv2 [11]) has alleviated the problem of water-like droplets in synthesized images. Although, the background of the face; accessories such as earrings, microphones, mold, and even emerging abnormal areas; and the structure around the face remain disorganized and unclear in a few cases. Similar to the conditional GAN (CGAN) [12], BigGAN [5] is another method for HQ image generation with image sizes of 128×128 , 256×256 , and 512×512 . It performs class-supervised training on the ImageNet, which is a large-scale dataset with 1000 classifications. These deep GANs have good performances for image generation but training them requires significant computational power and numerous image samples, indicating there is room to utilize pre-trained GANs for image-related tasks.

More importantly, there is no encoding ability in conventional GANs, indicating they cannot directly reconstruct images. This ability is called GAN inversion [13]. Previous works [14], [15] tried to add an encoder that is trained with the GANs. Such methods are effective in generating low-quality images (below 256×256) with shallow networks. However, they did not achieve high performances for deep GANs, which shows a failure to encode HQ images into single-type latent vectors or reconstruct images for higher fidelity. As one of the StyleGAN inversion methods, Image2StyleGAN [16] optimizes the style latent vector w (size of [18,512]) which replaces the general latent vector z (size of [1,512]), but each image should be optimized independently to attain its corresponding w . The In-Domain GAN [17] provides an encoder that trains with a discriminator to embed images into semantic vectors for GAN inversion. In addition, In-Domain GANs optimize real image w 's based on the encoder output. The ALAE [18] designs an auto-encoder framework to upgrade the StyleGAN and train it without pre-trained GANs to produce higher quality images with their reconstructions. The pSp [19] directly trains an encoder for StyleGAN to output image w 's via face identity loss. For BigGAN inversion and

This work was supported by the Science and Technology Development Fund (FDCT) of Macau under Grant No. 0016/2019/A1.

Cheng Yu is with the Faculty of Information Technology, Macau University of Science and Technology, Macau 999078, China. (E-mail: disanda@outlook.com)

Wenmin Wang is the corresponding author, with the International Institute of Next Generation Internet, and also with the State Key Laboratory of Lunar and Planetary Sciences, Macau University of Science and Technology, Macau 999078, China. (E-mail: wmwang@must.edu.mo.)

The code and pre-trained models are available at <https://github.com/disanda/MTV-TSA>.

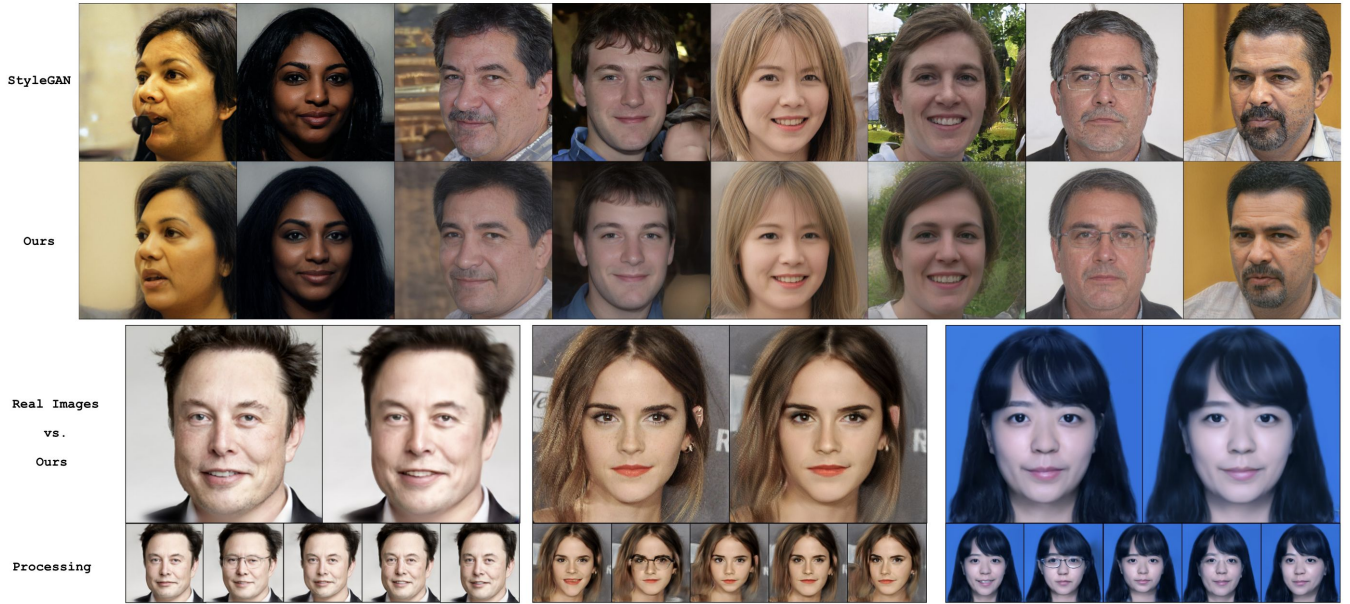


Fig. 1. The 1st row shows the face images generated by the pre-trained generator (StyleGANv1 [1] FFHQ 1014×1024). The 2nd row shows the reconstructed images using our method. Some reconstructions are better than the baseline by comparing the local details. The 3rd row shows the results for 3 pairs of real images (left) and their reconstructions (right). The 4th row shows the reconstructions process from 5 learned attribute directions (mouth, eyeglasses, younger, older, and pose).

drawing on the concept of BiGAN, BigBiGAN [20] improves the discriminator to judge image-latent pairs (rather than just judging images as in standard GANs) and trains the encoder with an upgraded BigGAN to obtain the BigGAN image reconstructions.

To summarize, these methods measure the divergence between generated images with their reconstructions and measure the divergence between their corresponding latent vectors. The mean square error (MSE) and learned perceptual image patch similarity (LPIPS) are generally selected [21] when comparing image divergence. To compare latent code divergence, the MSE is selected with the cosine similarity. In fact, assessing perceptual image quality is a difficult problem, and the PSNR and structural similarity index (SSIM) [22], [23], [24], [25], [26], [27], [28] are more commonly used to measure image divergence. Compared to LPIPS, the SSIM has a higher computational efficiency, and the SSIM [29] gives a much better indication of encoder training.

To compare HQ images, only measuring the image itself is insufficient, especially on misaligned images. On the other hand, HQ image embedding should better measure the latent vectors. One reason is that the image and latent vector sizes are too far apart. So, latent vectors cannot map images well. We divide the latent vectors into multi-scale vectors and add key image attentions. For the latent vector, similar to StyleGANs, we add more types (e.g., style latent vectors) for samples from the network data flow. For images, we extract two-scale attentions, which focus on important components of the target images.

Our work focuses on HQ image embedding and its reconstruction. We attempt to reconstruct images by creating a novel set of encoders based on pre-trained GANs, which help GANs map HQ images to multi-type latent vectors. Therefore,

we reorganize the encoder and the generator to an auto-encoder when we treat the former GAN generator as a decoder. Inspired by [1], we design a general block that contains two convolutional layers. We try to match different GANs using the fine-tune block, which is designed to construct each down-sampling block of encoders. Finally, we offer a novel method that reconstructs HQ synthesized and real images with a high fidelity while improving and maintaining the image qualities. Our encoder guarantees the semantic attributes attached to the latent vectors. With the current methods of semantic directions, such as supervised training via attribute classification machine [30], we can use the learned directions to change image attributes. The contributions of our work can be summarized as follows:

- For image reconstruction, we design a set of encoders to adapt deep GANs. Fine-tuning the block designed to match different GANs allows training the encoders using corresponding pre-trained GANs with few additional training costs (within 7 epochs). To the best of our knowledge, the proposed encoders are the first sets that adapt well in current state-of-the-art GANs (including PGGAN, StyleGANv1, StyleGANv2, and BigGAN).
- To better embed HQ images to latent vectors, we both expand valuable ranges in images with their corresponding latent vectors and divide latent vectors as multiple types while extracting two-scale attentions from images. We divide aligned images into three overlapping regions using the attention mechanism to highlight the important parts of images to better embed latent vectors to enhance the reconstruction fidelity. For misaligned images, we use Grad-CAM to find key target positions and use those positions to make two-scale attentions.

- To train encoders, we revisit the measurement methods of similarity. We design two sets of loss functions based on similarity measurements. We use the MSE, information divergence, and cosine similarity to measure latent vectors. We then add two other methods (SSIM and LPIPS) to measure images and image attentions. The well-trained encoders with some additional training steps could reach higher performances in real image reconstruction. Furthermore, our method maintains semantic attributes in real images. Using latent directions from existing work [30] enables direct well-processed semantic attributes on real images (e.g., human faces).

II. RELATED WORK

A. Image Reconstruction in GANs

GANs play an essential role in image-related applications, such as real image reconstruction and processing, through image generation. For supervised learning, semantic labels as prior conditions in CGANs, such as StarGANs [31], [32] and ATT-GAN [33], could transform image semantic attributes into something else. However, real image reconstruction and attribute processing are difficult in unsupervised learning. The GAN inversion aims to faithfully reconstruct images from latent vectors using the generator [13]. The GAN inversion is also called image embedding or mapping, where image reconstruction depends on the GAN inversion. There are two ways to invert images to their latent vectors. One was proposed by Image2StyleGAN [16], which utilized a set of style latent vectors based on StyleGAN, and found the vector-specific values by training with corresponding images. The disadvantage of this method is that finding the w in any one image requires significant training operations (more than 10,000 epochs per image), making it less efficient when there are several images. We consider another way using encoders to accomplish this, which embeds the given images back into latent vectors from pre-trained GANs.

Specified image datasets can normally be treated as high-dimensional manifolds. The traditional size of latent vectors when designing an encoder to embed images into lower-dimensional vectors has fewer than 512 dimensions (i.e., latent vectors, which has also been called latent codes and latent variables with samples from latent space), such as the VAE, BiGAN, and PGGAN [34], [14], [4]. The HQ image mapping task cannot be performed in the latent vector as it is too small. This readily causes mode collapse or spatial entanglement in latent representation, such as for image reconstruction. Although there are methods to reduce spatial entanglement [35], [36] by sampling latent vectors on manifold directions, they can only solve this problem in a few certain cases. In StyleGAN, there are an additional 512-dimensional style latent vectors in each convolution layer besides the typical latent vector (i.e., general GAN input). Based on the larger latent size, the relationship between the latent vectors and image semantic attributes can be found in a supervised manner [30], which could also be discovered in unsupervised methods [37]. Furthermore, the image attribute process can be handled in learned attribute directions.

Existing methods [14], [20], [17], [18], [19] have successfully mapped images to latent vectors via encoders. These works have only matched a single-type GAN and limited reconstruction performance for real and misaligned images. The StyleGANv1, ALAE [18], In-Domain GAN [17], and pSp [19] map HQ images to latent vectors through the style latent vector, w . The In-Domain GAN attaches latent vectors to semantic information, and the ALAE implements an auto-encoder based on the StyleGAN to enable HQ image synthesis with corresponding reconstructions. The pSp adds identity loss to judge reconstructed face images. Motivated by BiGAN, the BigBiGAN [20] implements GAN inversion for BigGAN via an encoder. However, this does not explore the kernel relationship between reconstructing high-fidelity images with their latent presentation. These train one specific GAN while also training the encoder. To reduce training costs and enhance generalization, we train a set of encoders on pre-trained GANs.

The traditional auto-encoder can realize the mapping relationship between low-quality images using single-type vectors (e.g., VAE [34]). However, training an encoder to reconstruct HQ images is difficult. On one hand, the HQ image size is too large, which is usually up to 1024×1024 pixels. When images are mapped to lower-dimensional vectors, the mapping relationship becomes intricate due to the massive size gap. Consequently, the latent space cannot represent image information accurately because of information loss in the dimension reduction. We reduce the gap by extracting two-scale attentions from high-dimensional information and divide the latent space into multi-type vectors.

B. Similarity Measurement

In existing methods, LPIPS has been widely used to measure the similarities between images and their reconstructions. To measure the perceptual similarity, LPIPS requires a pre-trained model (e.g., VGG [38] or AlexNet [39]), which is trained from ImageNet [40] to extract multiple-layer features from images. To better address the difficulties of HD image reconstruction, we add two improvements based on LPIPS.

1) *SSIM Index*: Reconstructed images are subject to inevitable distortions in deep neural networks, such as passing the down- or up-sampling layer, including the convolutional, normalization, pooling, and activation layers. Any of these layers may degrade the reconstruction quality. We consider the SSIM [29] to measure the perceptual similarities of images with their reconstructions. The SSIM has a high computational efficiency and does not require pre-training.

2) *Grad-CAM*: Zhou et al. [41] proposed a technique called class activation mapping (CAM) to locate target positions within images using the ImageNet model. However, to obtain locations, CAM needs to train the model again, which removes the fully connected layers from the model output. The Grad-CAM [42] upgrades the CAM method by utilizing a pre-trained model gradient at the pixel level and does not require retraining the model. We force the Grad-CAM and LPIPS to use the same ImageNet model (VGG). Then, one result (LPIPS) is obtained through forward propagation, and the other (Grad-CAM) is obtained through backpropagation.

III. MULTI-TYPE VECTORS WITH TWO-SCALE ATTENTIONS

There is a subtle relationship between different latent vectors and images. Embedding HQ images into latent space via encoders is a complex process. We achieve an ideal mapping relationship by constructing a set of loss functions between the latent vectors and images. To enhance the mapping effect, we divide latent vectors into multi-type vectors (MTV). Moreover, we adopt a mechanism called two-scale attentions (TSA) that is used to locate target positions in images, and the MTV-TSA can be treated as a multiple-objective optimization that carries additional feature information. Therefore, to better embed images into latent vectors, we design the TSA from the images. To ensure latent vectors better represent images, we expand the single latent type into multi-types so that the embedded MTV can better reflect the feature information.

In the MTV-TSA, the mapping relationship becomes more complex, which we realize using two sets of loss functions. To measure the similarity of latent vectors, we leverage the cosine similarity, information divergence, and MSE. To measure images and their attention similarities, we primitively unify gradient-weighted class activation mapping (Grad-CAM) to extract misaligned image attentions and add SSIM with LPIPS to measure the similarity.

A. Multi-type Vectors (MTV) on Latent Space

In common generative models such as GANs or auto-encoders, we only sample latent vectors (LV) from a single type of distribution to embed image vectors (IV) into the LV. The specific distribution of the LV could also be called the latent space. We denote LV as z , which obeys a Gaussian distribution. We briefly regard a one-type LV as obeying the same distribution, and we denote IV as x , which obeys the statistical distribution of a pre-trained generator output. Moreover, we denote the ground truth images as y , which obeys the distribution of a large-scale image dataset. The optimization goal for GANs can be treated as $x \sim y$. In normal GAN inversions, there are one-type LV z' , which come from an encoder and could be used to reconstruct images x' . We denote an encoder as E , and we treat a pre-trained generator G as a decoder.

As shown in Eq. 1, we apply the encoder loss function between the two vector-pairs, image vector-pairs ($x = G(z), x'$), and latent vector-pairs ($z, z' = E(x')$) as

$$\mathcal{L}_E = \mathcal{L}_{LV}(x, x') + \mathcal{L}_{IV}(z, z'). \quad (1)$$

To upgrade the encoder parameters, we compare the similarities in the vector-pairs, such as (x, x') and (z, z') . If the vector size is $z \ll x$, the mapping is too intricate to perform. For HQ image datasets, the IV do not map well into single-type LV, so the LV cannot achieve ideal representation for high-dimensional data, such as the general latent vector z , which should map an image size of $(n, 3, 1024, 1024)$ to a latent vector of size $(n, 512)$. Here, n is training batch size.

In StyleGANs, which is similar to recent GAN inversion works [1], [18], [16], [19], [17], we expand the latent vector

size $z: (n, 512)$ to $w: (n, n_{layers}, 512)$. The w is the layer-level style vector that comes from each convolutional layer, and n_{layers} is the number of convolutional layers in G (e.g., 1024×1024 images need 18 convolutional layers in StyleGANs). Unlike other methods, we add two other types of LV that have different dimensional sizes to participate in the mapping. To stabilize the training process and enhance the performance of latent representation based on the tremendous gap between the image and latent vector sizes, the one added latent vector is constant with input vectors z_c , where the size of z_c is $(n, 512, 4, 4)$. The z_c is used to first block the input in StyleGANs' G , where the size of z_c is larger than the general GAN input (z). The other is the layer-lever noise vector z_n , which is performed as learning able parameters on each convolutional layer, where z_n is of size $(n, n_{layers}, n_{channels})$. The $n_{channels}$ represents the number of input channels for each convolutional layer.

We use E to output w' , which should imitate w , to obtain the vector-pairs (w, w') and increase their similarity via encoders. The other latent vector-pairs operate the same way. Next, we form the 3 single-type latent vector-pairs $((w, w'), (z_c, z'_c), (z_n, z'_n))$ together and call them multi-type vectors (MTV). The embedding loss function for the MTV is as follows:

$$\mathcal{L}_{LV}(z, z') \rightarrow \mathcal{L}_{MTV}((w, w'), (z_c, z'_c), (z_n, z'_n)). \quad (2)$$

With this change, the LV are compared with their reconstructions, which include the constant input vectors z_c , random noise vectors z_n , and style LV w . Compared with the baseline, which only uses single-type LV (z or w), the contained feature information from the MTV is further enlarged. The z_c enhances the stability of the image embedding, and z_n benefits for the diversity of the latent representation, which occurs in the local details of HQ images.

We measure the MTV similarity with a set of loss functions. All latent vector types are measured in the same way, such as the vector-pair (w, w') . We set the batch size of vectors to n , and first use the MSE and cosine similarity. The loss functions are summarized as follows:

$$\begin{aligned} \mathcal{L}_{MTV}(w, w') &= \mathcal{L}_{mse}(w, w') + \mathcal{L}_{cos}(w, w') \\ &= \frac{\|w - w'\|_2}{n} + 1 - \frac{w \cdot w'}{\|w\|_2 \times \|w'\|_2}. \end{aligned} \quad (3)$$

We analyze the vector similarity from a statistical perspective and measure it on the same distribution. We measure the distribution similarity for each vector-pair and add the Kullback–Leibler (KL) divergence (also called information divergence). We add an activation function (SoftMax, \mathcal{S}) to use the divergence measurement together with Eq. 3. We assume one-type vectors coming from the same distribution (i.i.d.), and let vectors pass \mathcal{S} when using the KL loss (see Eq. 4) as:

$$\mathcal{L}_{kl}(w, w') = - \sum_k^j \mathcal{S}(w') \log \frac{\mathcal{S}(w)}{\mathcal{S}(w')}, \quad (4)$$

Finally, we summarize the joint loss functions that measure the MTV similarity as:

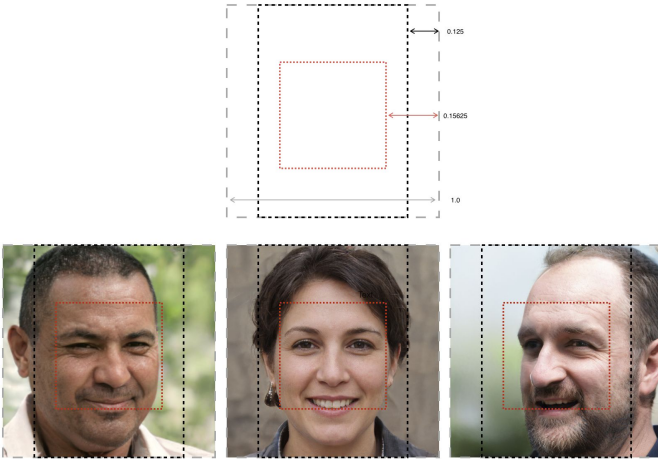


Fig. 2. Two-scale attention regions for aligned images. The gray dashed window is the actual scale of the image, the black dashed window is the first attention (AT1), and the red dashed window is the second attention (AT2).

$$\mathcal{L}_{MTV} = \mathcal{L}_{mse} + \mathcal{L}_{cos} + \mathcal{L}_{kl}. \quad (5)$$

Even though we have expanded LV types to reduce the gap between the LV and IV, the entire dimensional size of the LV is still smaller than the IV. So, we additionally consider reducing the training obstacles from the IV.

B. Two-scale Attentions (TSA) on Image

It is difficult to map HQ images to latent space while maintaining a high-fidelity reconstructed image. Information is inevitably lost not only after the encoding process but also after decoding. The most common phenomenon is that many local details become different in the reconstructed images, especially for HQ images. Therefore, we add the TSA from images to reach higher fidelities when reconstructing images to be as similar to the original image as possible.

The other two attention vectors are taken from the IV (x). We denote the two attentions as x_1 and x_2 . These are distilled using specific extraction rules defined by their reconstructions as: $x_1, x'_1 = AT1(x, x')$ and $x_2, x'_2 = AT2(x, x')$. Finally, we expand the one-type image vector-pair (x, x') to three vector-pairs ((x, x') , (x_1, x'_1) , (x_2, x'_2)), which contain images vectors with their TSA. The TSA sizes are smaller or equal to the IV, but the TSA is outstanding for its key target features, which further reduces the mapping obstacles between the IV and their LV. Such changes improve the mapping performance for auto-encoding. The loss function for the TSA is given as:

$$\mathcal{L}_{IV}(x, x') \rightarrow \mathcal{L}_{TSA}((x, x'), (x_1, x'_1), (x_2, x'_2)). \quad (6)$$

For preprocessed datasets (e.g., face images from CelebA-HQ [43] and FFHQ [1]), images are aligned and the targets are located in the image centers. Thus, the TSA is simple for aligned images, such as human faces. As shown in Fig. 2, we strengthen the TSA in two key regions. The first attention (AT1) is the region where the target is concentrated for human perception, which is enclosed in the black dashed line. Based

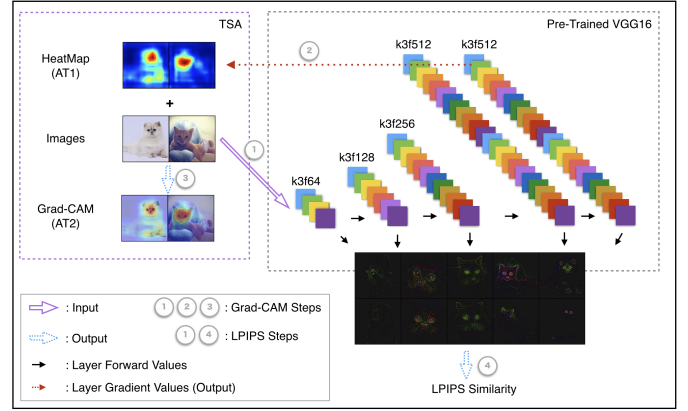


Fig. 3. Two-scale attentions for misaligned images. The first attention comes from image heat maps as obtained from the pre-trained VGG16 (AT1), and the second attention comes from IV with their heat maps (AT2).

on AT1, we established the second region (red dashed line) as the second attention (AT2) to further strengthen the target-centered details for face images. This simple technique is particularly effective when images are aligned to the center. We give a suitable ratio of face images with the TSA as (1: 0.75: 0.6875).

To handle misaligned images, we use the Gram-CAM-based TSA to find the key regions. As shown in Fig. 3, we place images into the VGG16 [38] model, which contains 5 blocks with 13 convolutional layers that are pre-trained from ImageNet. After the model is forward propagated, we extract the gradient values from the last convolutional layer of the last block to generate the image heat maps. These can position the image target, and we denote this process as $x_1, x'_1 = AT1(x, x')$. Furthermore, we place target positions (from heat maps) into IV at the pixel level to obtain the Grad-CAM vectors. This process is expressed as $x_2, x'_2 = AT2(x, x')$.

Apart from the MTV loss functions, we add two new loss functions to the TSA: the LPIPS [21] and SSIM [29]. We reuse the VGG16 model to obtain the LPIPS and select the final convolutional layer in each block of the model to extract image features and compute the feature MSE for the LPIPS. Next, we directly use [29] to acquire the SSIM results. The entire TSA loss function is as follows:

$$\mathcal{L}_{TSA} = \mathcal{L}_{mse} + \mathcal{L}_{cos} + \mathcal{L}_{kl} + \mathcal{L}_{lpiips} + \mathcal{L}_{ssim}. \quad (7)$$

Finally, the loss function for the MTV-TSA to train encoders can be briefly summarized as:

$$\mathcal{L}_E = \mathcal{L}_{TSA} + \mathcal{L}_{MTV}. \quad (8)$$

IV. ENCODER DETAILS AND IMPLEMENTATION

We illustrate the pipeline of vector-pairs in Fig. 4 for StyleGANs. Here, we fix the weights of the generator G and regard it as a decoder before training E . The architecture of E is nearly symmetric to G . The (w, z_c, z_n) input to G and (w', z'_c, z'_n) come from E , and the block architecture of E is shown in Fig. 5. We select the residual bypass in each block, where the block architecture contains two convolutional layers

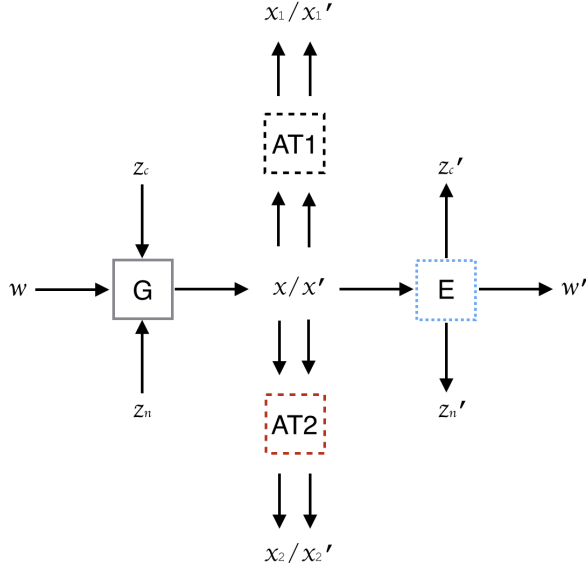


Fig. 4. Vector flow of the StyleGAN MTV-TSA with three types of image vector-pairs in the TSA and three types of latent vector-pairs in the MTV.

(CONV). Based on the CONV, we obtain the noise vector z'_n from the learnable weights and determine the style vectors w' from the fully connected layers (FC). The FC and CONV are based on an equalized learning rate [4]. We initialize the weights using the Xavier norm [44]. The details of the entire architecture of E are given in Table I.

To perform the PGGAN E , we remove the style- and noise-related vectors with their corresponding layers and weights (i.e., FC for w' and learnable weight z'_n). We then change the second CONV to an FC in the last block of E to adapt to different GAN outputs. Distinct from StyleGANs, the output size of D ($z'_c \in \mathbb{R}^{512 \times 4 \times 4}$) is adjusted to the input size of the PGGAN G ($z \in \mathbb{R}^{512}$).

To perform the BigGAN E , we remove the w' and relevant layers from each block. We replace the instance norm with the conditional batch normalization (CBN). We then add condition vectors and treat them as $c \in \mathbb{R}^{256}$, before placing c into CBN. The c additionally contains the image-class information and is an input into G to synthesize the corresponding images. The CBN has no learnable weight (constant mean and variance). Two FC layers separately output the c' and $z'_c \in \mathbb{R}^{128}$ in the last block of E . Additional architecture details for E (PGGAN and BigGAN) are reported in Table II.

The encoder training is performed in a self-supervised manner. A large number of random samples (z) is used to decode and obtain $G(z) \simeq x$. The x with its reconstructions $x' \simeq G(E(G(z)))$ constitute the image vector-pair (x, x') . In pre-trained GANs, $G(z)$ significantly exceeds the dataset samples y . So, we replace the training sample y with $G(z)$, which does not require any dataset samples. Based on self-supervised learning (SSL), we obtain more data inputs than from the GAN training. We set the number of random samples to 30,000 times the batch size to train the encoders. The (x_1, x'_1) and (x_2, x'_2) are resized to match (x, x') . To summarize the implementation, we present the details in Algorithm 1 and take the StyleGAN

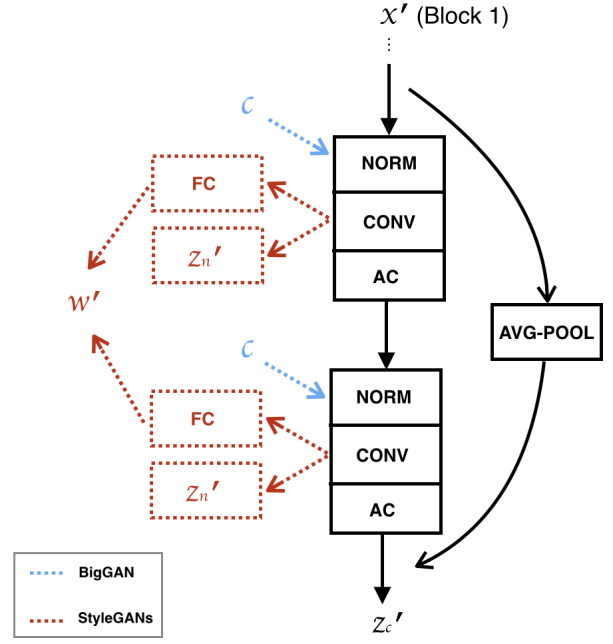


Fig. 5. Overview of the one block architecture for E . We denote the normalization layer as NORM, activation layer as AC, and fully connected layer as FC. The FC (output w') and z'_n weights are not used in the PGGAN or BigGAN.

Algorithm 1 Training Encoders via MTV-TSA (SSL)

Input: z, z_c, z_n . **Fixed weight:** G, M .

Training: E on its weight $\rightarrow w_E$

Begin:

- 1: **while true do**
- 2: Sample: $z \sim N(0, 1)$.
- 3: Forward Nets: $w = M(z), x, z_c, z_n = G(w)$.
- 4: Attentions: $x_1 = AT_1(x), x_2 = AT_2(x)$.
- 5: **if** $x \sim G(E(x))$ **then**
- 6: Return.
- 7: **else**
- 8: $x' = G(E(x)), x'_1 = AT_1(x'), x'_2 = AT_2(x')$.
- 9: $w', z'_c, z'_n = E(G(E(x)))$.
- 10: $\nabla \mathcal{L}_1 \leftarrow \mathcal{L}_{TSA}((x, x'), \mu_1(x_1, x'_1), \mu_2(x_2, x'_2))$
- 11: $\nabla \mathcal{L}_2 \leftarrow \mathcal{L}_{MTV}(\nu_1(w, w'), \nu_2(z_c, z'_c), (z_n, z'_n))$
- 12: $w_E \leftarrow w_E + \nabla \mathcal{L}_1 + \nabla \mathcal{L}_2$
- 13: **end if**
- 14: **end while**
- 15: **Output:** E, x'

End

as an example. We use the general latent vector $z \in \mathbb{R}^{512}$, which is placed into the pre-trained mapping model M to obtain initial style latent vector $w \in \mathbb{R}^{512 \times n_{layers}}$.

Here, we set ν_1 and ν_2 to 0.01 and offer two cases to set (μ_1, μ_2) and E . In the training results, larger (μ_1, μ_2) gives slightly better performances (optimization focused on the attention-related regions). In case 1, we set $\mu_1 = 1$ and $\mu_2 = 1$ and only use two attentions to improve the auto-encoding performance. To save GPU memory, we remove the gradients

TABLE I
ENCODER ARCHITECTURES FOR STYLEGANs.

Block ID Res.	StyleGANs' Encoder (E)		
	256×256	512×512	1024×1024
1 4×4	FC, IN, CONV(64,64,3), P_{z_n} , L-ReLU	FC, IN, CONV(32,32,3), P_{z_n} , L-ReLU	FC, IN, CONV(16,16,3), P_{z_n} , L-ReLU
	FC, IN, CONV(64,128,3), P_{z_n} , L-ReLU	FC, IN, CONV(32,64,3), P_{z_n} , L-ReLU	FC, IN, CONV(16,32,3), P_{z_n} , L-ReLU
2 8×8	FC, IN, CONV(128,128,3), P_{z_n} , L-ReLU	FC, IN, CONV(64,64,3), P_{z_n} , L-ReLU	FC, IN, CONV(32,32,3), P_{z_n} , L-ReLU
	FC, IN, CONV(128,256,3), P_{z_n} , L-ReLU	FC, IN, CONV(64,128,3), P_{z_n} , L-ReLU	FC, IN, CONV(32,64,3), P_{z_n} , L-ReLU
3 16×16	FC, IN, CONV(256,256,3), P_{z_n} , L-ReLU	FC, IN, CONV(128,128,3), P_{z_n} , L-ReLU	FC, IN, CONV(64,64,3), P_{z_n} , L-ReLU
	FC, IN, CONV(256,512,3), P_{z_n} , L-ReLU	FC, IN, CONV(128,256,3), P_{z_n} , L-ReLU	FC, IN, CONV(64,128,3), P_{z_n} , L-ReLU
4 32×32	FC, IN, CONV(512,512,3), P_{z_n} , L-ReLU	FC, IN, CONV(256,256,3), P_{z_n} , L-ReLU	FC, IN, CONV(128,128,3), P_{z_n} , L-ReLU
	FC, IN, CONV(512,512,3), P_{z_n} , L-ReLU	FC, IN, CONV(256,512,3), P_{z_n} , L-ReLU	FC, IN, CONV(128,256,3), P_{z_n} , L-ReLU
5 64×64	FC, IN, CONV(512,512,3), P_{z_n} , L-ReLU	FC, IN, CONV(512,512,3), P_{z_n} , L-ReLU	FC, IN, CONV(256,256,3), P_{z_n} , L-ReLU
	FC, IN, CONV(512,512,3), P_{z_n} , L-ReLU	FC, IN, CONV(512,512,3), P_{z_n} , L-ReLU	FC, IN, CONV(256,512,3), P_{z_n} , L-ReLU
6 128×128	FC, IN, CONV(512,512,3), P_{z_n} , L-ReLU	FC, IN, CONV(512,512,3), P_{z_n} , L-ReLU	FC, IN, CONV(512,512,3), P_{z_n} , L-ReLU
	FC, IN, CONV(512,512,3), P_{z_n} , L-ReLU	FC, IN, CONV(512,512,3), P_{z_n} , L-ReLU	FC, IN, CONV(512,512,3), P_{z_n} , L-ReLU
7 256×256	FC, IN, CONV(512,512,3), P_{z_n} , L-ReLU	FC, IN, CONV(512,512,3), P_{z_n} , L-ReLU	FC, IN, CONV(512,512,3), P_{z_n} , L-ReLU
	FC(1024,512)	FC, IN, CONV(512,512,3), P_{z_n} , L-ReLU	FC, IN, CONV(512,512,3), P_{z_n} , L-ReLU
8 512×512		FC, IN, CONV(512,512,3), P_{z_n} , L-ReLU	FC, IN, CONV(512,512,3), P_{z_n} , L-ReLU
		FC(1024,512)	FC, IN, CONV(512,512,3), P_{z_n} , L-ReLU
9 1024×1024			FC, IN, CONV(512,512,3), P_{z_n} , L-ReLU
			FC(1024,512)

* In CONV(C_{in}, C_{out}, K), C_{in} is the input channel, C_{out} is the output channel, and K is the kernel size. The stride and padding are 1 for all CONVs. The IN is instance normalization [45], L-ReLU is the activation function of the Leaky ReLU, and P_{z_n} is a learnable weight of size C_{in} . The FC outputs the style vectors, w' . In each layer, the FC (input and output nodes) size is ($C_{in} \times 2, 512$).

* In block 1 of E , CONV(3, C_{in} , 1) is not shown in the table, which maps the RGB channels to C_{in} . The average pooling layer (AVG-POOL) in each block is also not shown.

TABLE II
ENCODER ARCHITECTURES FOR PGGAN AND BIGGAN

Block ID Res.	PGGAN's Encoder (E)	BigGAN's Encoder (E)	BigGAN's Encoder (E)
	256×256		512×512
1 4×4	IN, CONV(64,64,3), L-ReLU	CBN, CONV(64,64,3), L-ReLU	CBN, CONV(32,32,3), L-ReLU
	IN, CONV(64,128,3), L-ReLU	CBN, CONV(64,128,3), L-ReLU	CBN, CONV(32,64,3), L-ReLU
2 8×8	IN, CONV(128,128,3), L-ReLU	CBN, CONV(128,128,3), L-ReLU	CBN, CONV(64,64,3), L-ReLU
	CONV(128,256), IN, L-ReLU	CBN, CONV(128,256,3), L-ReLU	CBN, CONV(64,128,3), L-ReLU
3 16×16	IN, CONV(256,256), L-ReLU	CBN, CONV(256,256,3), L-ReLU	CBN, CONV(128,128,3), L-ReLU
	IN, CONV(256,512), L-ReLU	CBN, CONV(256,512,3), L-ReLU	CBN, CONV(128,256,3), L-ReLU
4 32×32	IN, CONV(512,512), L-ReLU	CBN, CONV(512,512,3), L-ReLU	CBN, CONV(256,256,3), L-ReLU
	IN, CONV(512,512), L-ReLU	CBN, CONV(512,512,3), L-ReLU	CBN, CONV(256,512,3), L-ReLU
5 64×64	IN, CONV(512,512), L-ReLU	CBN, CONV(512,512,3), L-ReLU	CBN, CONV(512,512,3), L-ReLU
	IN, CONV(512,512), L-ReLU	CBN, CONV(512,512,3), L-ReLU	CBN, CONV(512,512,3), L-ReLU
6 128×128	IN, CONV(512,512), L-ReLU	CBN, CONV(512,512,3), L-ReLU	CBN, CONV(512,512,3), L-ReLU
	IN, CONV(512,512), L-ReLU	CBN, CONV(512,512,3), L-ReLU	CBN, CONV(512,512,3), L-ReLU
7 256×256	IN, CONV(512,512), L-ReLU	CBN, CONV(512,512,3), L-ReLU	CBN, CONV(512,512,3), L-ReLU
	FC(512×4×4,512)	FC(512×4×4,256), FC(256,128)	CBN, CONV(512,512,3), L-ReLU
8 512×512			CBN, CONV(512,512,3), L-ReLU
			FC(512×4×4,256), FC(256,128)

* PGGAN has neither w or z_n , and its E outputs $z'_c \in \mathbb{R}^{512}$.

* BigGAN has no w . Its E outputs the conditional vector $c' \in \mathbb{R}^{256}$ and the latent vector $z'_c \in \mathbb{R}^{128}$. The CBN is the conditional batch normalization [5] used for the BigGAN generator. This requires one-hot classification vectors c as its input.

of the G output when training backward propagations. In addition, removing the G output gradients create different performances. In case 2, we set $\mu_1 = 5$ and $\mu_2 = 9$ and retain the fused scale operations, which are used in StyleGANs and PGGAN (additional blur operation in each convolutional block). The reconstructed images in case 2 are more faithful to the original images with a slight blur in the margins; however, keeping the image and attention gradients will increase the device consumption. In case 1, the reconstructed results begin changing from the other images, but in case 2, the reconstructed results start changing from noise and become blurred. We set case 1 as the default and only use case 2 in the StyleGANv1’s FFHQ faces (1024×1024) and LSUN’s cars (resize to 512×512) [46].

V. EXPERIMENTAL SECTION

To evaluate the MTV-TSA, we compare the pre-trained GAN generations to the MTV-TSA reconstructions (x vs. x'), including PGGAN,¹ StyleGANv1,² StyleGANv2,³ and BigGAN.⁴ We then compare the MTV-TSA with three closely related works: In-Domain GAN⁵ [17], ALAE⁶ [18], and pSp⁷ [19]. Furthermore, we perform an ablation study with different vectors (LV and IV) and report the training details. Finally, we demonstrate the real image process based on the MTV-TSA. All experiments were implemented (or re-implemented) on PyTorch as cited in the footnotes. The E is trained using the Adam optimizer [47] with a learning rate of $lr = 0.0015$, and decayed β of ($\beta_1 = 0$, $\beta_2 = 0.99$). The batch sizes (B) for different image sizes are $B_{256 \times 256} = 8$, $B_{512 \times 512} = 4$, and $B_{1024 \times 1024} = 2$. These sizes are trained on a GPU card (Nvidia Tesla V100-SXM3 32 GB).

A. Comparing Pre-trained GANs

We compare the GAN and MTV-TSA in Figs. 6 and 7. The MTV-TSA results are sampled from the 7 epochs with a batch size of $30,000 \times B$. In the PGGAN, we note that the reconstructions are better than the corresponding images, which are shown in rows 1 and 2 in Fig. 7. We believe that this improvement is based on additional training in the MTV-TSA. In StyleGANv1, the x' are slightly more blurred than x in LSUN car, which we believe is caused by highlighting the two attentions and performing blurring operations in the encoder setting for case 2 (see encoder details). The MTV-TSA reconstructs StyleGANs well for the LSUN cats and horses and repairs local areas if they are crumbled or produce unreasonable objects. In StyleGANv2, the MTV-TSA could perfectly reconstruct face images based on the high-performance x . Compared with the GAN results, the FID score does not improve in the reconstructions, and the MTV-TSA maintains the same level as the corresponding GANs.

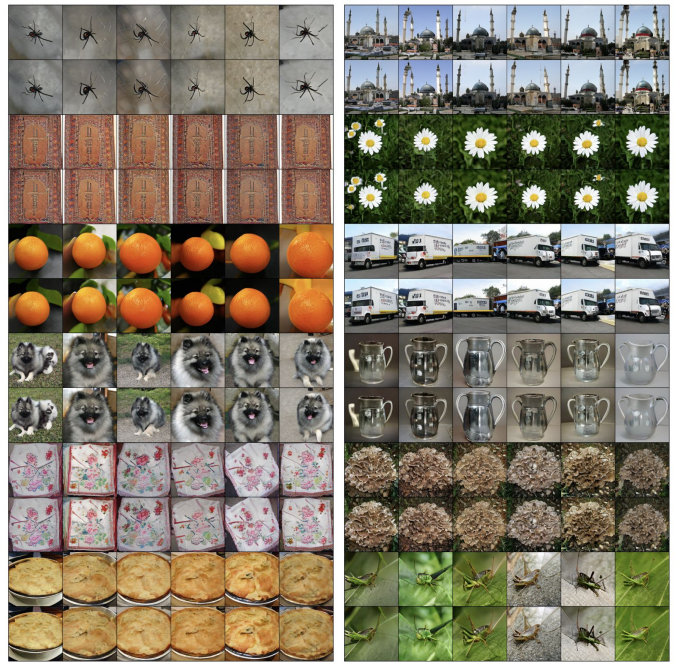


Fig. 6. BigGAN results (upper) with their reconstructions (lower) via MTV-TSA with a size of 256×256 .

TABLE III
COMPARISON OF SIMILARITIES BETWEEN SYNTHESIZED AND REAL IMAGES AND THEIR RECONSTRUCTIONS.

Synthesized Img	PSNR \uparrow	SSIM \uparrow	MSE \downarrow (e^2)	LPIPS \downarrow	CS \uparrow
ALAE	15.68	0.497	20.24	0.485	0.77
pSp	21.53	0.640	5.17	0.398	0.94
In-domain (R)	19.53	0.584	8.96	0.422	0.90
MTV-TSA (R)	20.45	0.630	6.67	0.368	0.92
<hr/>					
Real Img					
pSp	21.38	0.649	5.12	0.416	0.95
In-domain (R)	19.51	0.599	7.83	0.427	0.92
In-domain (I)	23.45	0.672	3.37	0.367	0.97
MTV-TSA (R)	19.12	0.601	8.57	0.421	0.91
MTV-TSA (OE)	25.92	0.767	1.76	0.293	0.98
<hr/>					
Identical Images	∞	1.000	0.00	0.000	1.00

In BigGAN, the MTV quickly converged in the optimization (within 5 epochs). The reconstructions are nearly the same as the synthesized images. We suspect this is due to the additional input of the condition vectors (c) in each CBN layer.

B. Comparing Related Works

To compare the baseline, we focus on real image reconstructions based on the pre-trained styleGANv1 (trained on an FFHQ of size 1024×1024). As shown in Fig. 8, the reconstructions of the ALAE and pSp are taken directly from pre-trained encoders. The In-Domain (R) is also directly taken from its pre-trained encoder. Similar to Image2StyleGAN [16], In-Domain (I) optimizes w based on the In-Domain (R) results (default optimization time is 100). Similar to the In-Domain

¹PGGAN: https://github.com/akanimax/pro_gan_pytorch

²StyleGANv1: <https://github.com/podgorskiy/StyleGan>

³StyleGANv2: <https://github.com/genforce/genforce>

⁴BigGAN: <https://github.com/huggingface/pytorch-pretrained-BigGAN>

⁵In-Domain GAN: https://github.com/genforce/idinvert_pytorch

⁶ALAE: <https://github.com/podgorskiy/ALAE>

⁷pSp: <https://github.com/eladrich/pixel2style2pixel>

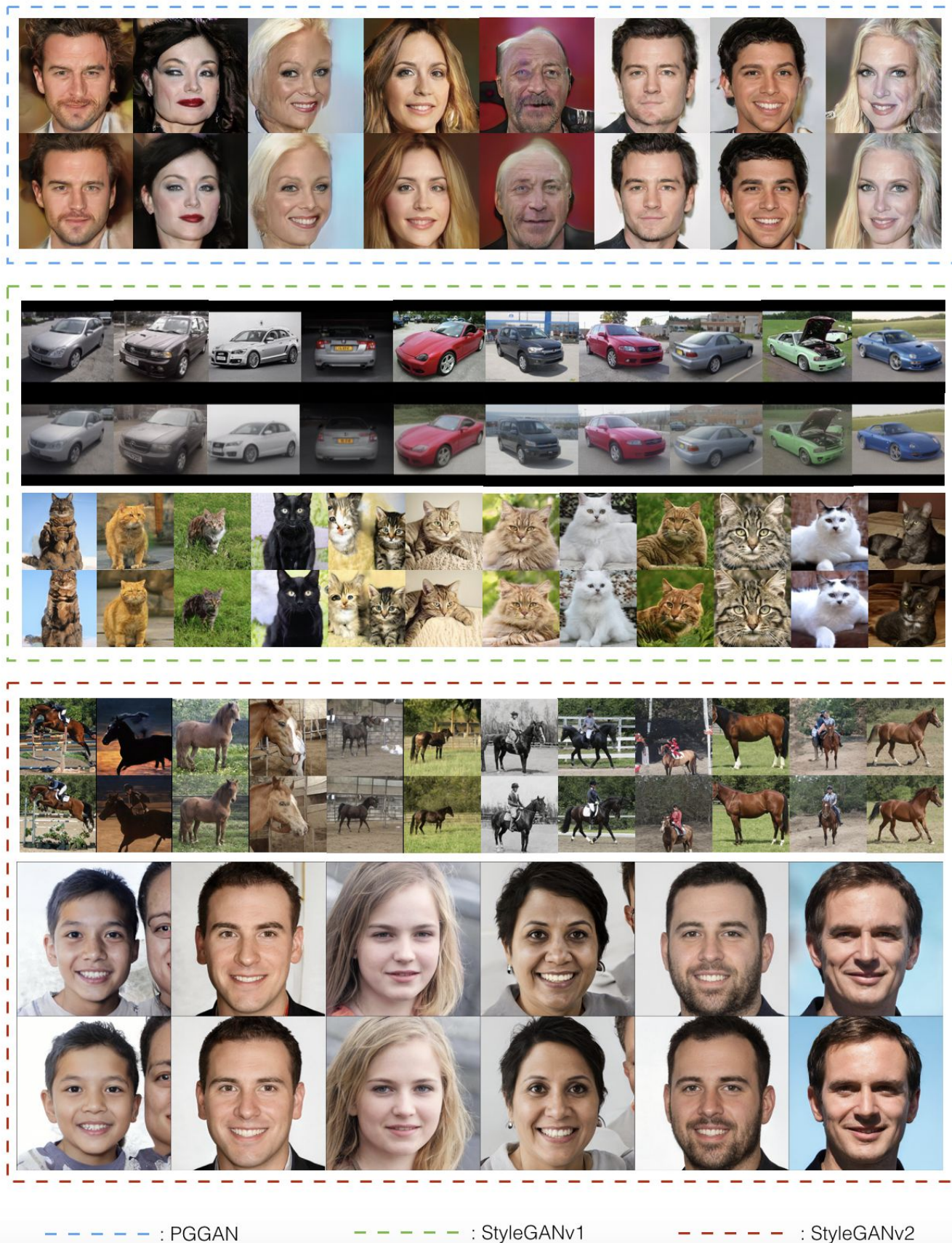


Fig. 7. The 1st row shows face images generated from the pre-trained PPGAN (CelebA-HQ 1024×1024). We see that some reconstructions (2nd row) are better than the baseline by comparing the local details. The 3rd and 5th rows show the StyleGANv1 results from LSUN [46] for cars (512×512) and cats (256×256). The 7th and 9th rows show the StyleGANv2 results with LSUN for horses (256×256) and FFHQ [1] face images (1024×1024). Their lower rows are the corresponding reconstructions using the MTV-TSA.

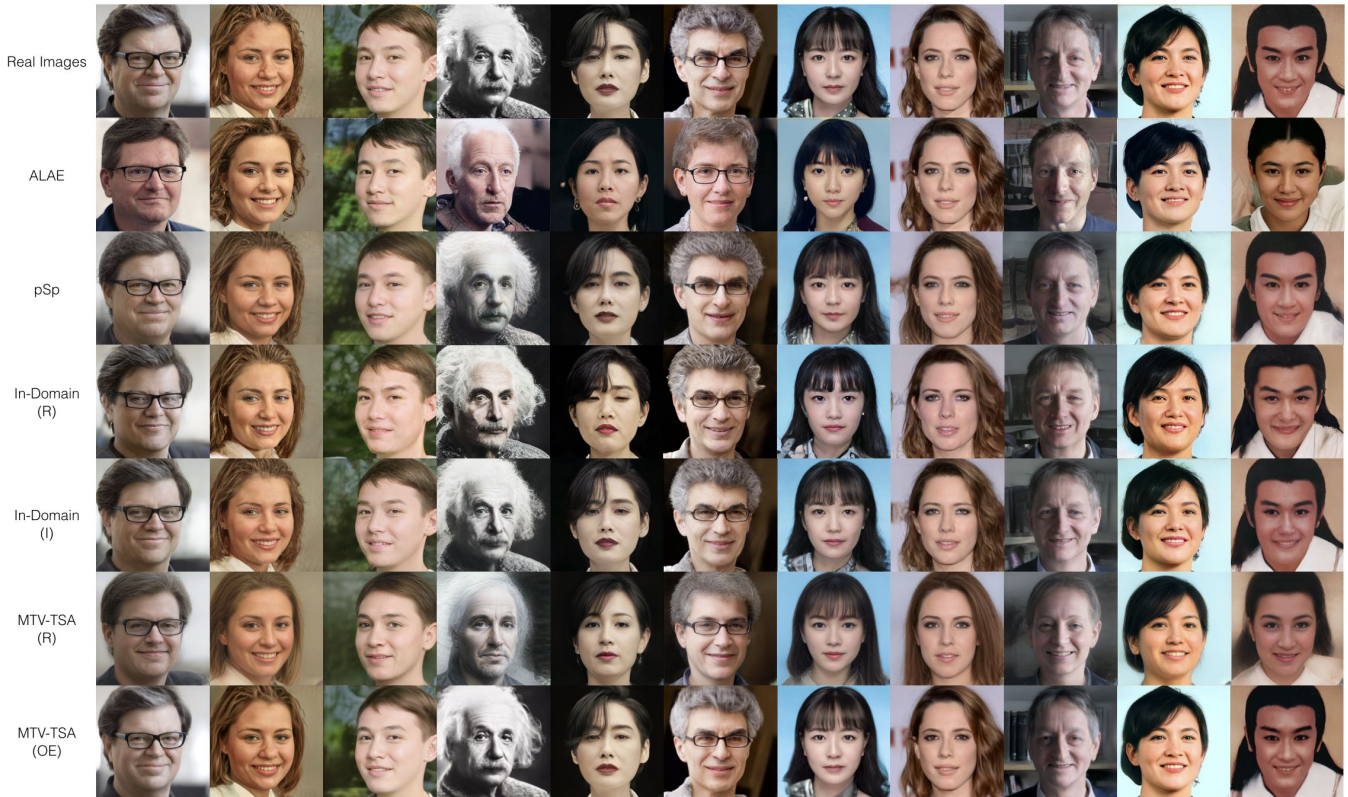


Fig. 8. Comparing the baseline to the MTV-TSA on real image reconstruction. The results of the ALAE , pSp, In-Domain (R), and MTV-TSA (R) are directly sampled from pre-trained encoders. The results of In-Domain (I) are sampled from further optimizations on w , and the MTV-TSA (OE) are sampled from further optimizations on E .

(R), the MTV-TSA (R) is also directly taken from its pre-trained encoder, but the MTV-TSA (OE) does not directly optimize w . Instead, it optimizes the pre-trained encoder and lets the encoder determine the ideal w . Therefore, the performance of the MTV-TSA (OE) is better and depends on a few more optimization iterations. To obtain ideal reconstructions, we further optimize the encoder 1,500 times. We also test the reconstruction similarity on the StyleGAN1 synthesized images and real images independently (3,000), where the real images are sampled from CelebAAMask-HQ [43]. Both results are reported in Table III. The pSp provides better results for GAN-synthesized images and is also good for real images. After additional training, the In-Domain (I) is limited by further optimizing a single latent style vector, but the MTV-TSA (OE) provides better performances by further optimizing its pre-trained encoder.

C. Ablation Study

Initially, we select the pre-trained GAN of StyleGANv1 (FFHQ 1024×1024 , $n_{layers} = 18$) and the corresponding results at an early epoch (4th with batch size 60,000) to evaluate the usages of MTA and TSA.

In generative models, mapping high-quality images to a smaller-sized latent space easily causes spatial entanglement. We compare the mapping relationships between different latent vector types without any attentions, which are z , $w/2$, w , z_c , and z_n . Different from the size of z_c . The z is the

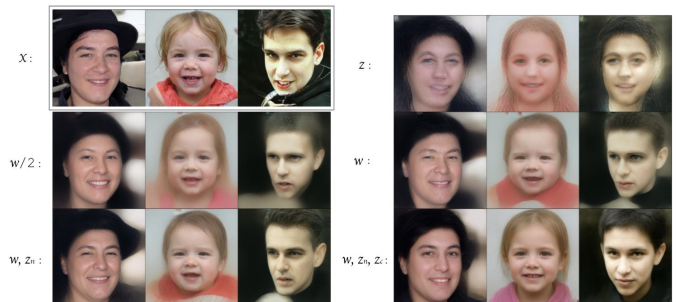


Fig. 9. Ablation study on MTV for different latent vector types. Without image attentions, differences can be easily observed in the examples.

common GAN input with size. The w is the latent style vector that involves all convolutional layer styles, and $w/2$ is only half of w and contains half of the layer styles, $(n, 9, 512)$. We sample z from a normal distribution $z \sim N(0, 1)$ and obtain $w/2$, w , and z_c from the pre-trained GANs. Their corresponding vectors output from E form vector-pairs to judge the similarities via Eq. 7. We then train the encoders based on different latent vector types. When additional types of latent vector-pairs are added to the mapping task, the clarity of the reconstructions is further improved, but the appearance of the reconstructed image will be slightly different from the target face after the latent types add z_c and z_n , as shown in the last line of Fig. 9.

Next, we consider enhancing the reconstruction similarity



Fig. 10. The 1st row demonstrates face images generated by the pre-trained generator (config F of StyleGANv1 [1]). The 2nd–4th rows demonstrate the reconstructed images by training with different attentions. Most reconstructions are very similar to the original face images when progressively adding one-scale attentions (AT1) and two-scale attentions (AT1 with AT2).

via image attentions. We reconstruct images while separately adding different center-aligned attentions (AT1 and AT2) for comparison. We choose the all-latent vector types (w , z_c , z_n) to optimize the encoders. As shown in Fig. 10, the encoder training includes different attention scales, which improves the performance of image reconstruction. We first add the AT1 vector-pairs (x_1 , x'_1) with reconstructed images to optimize the encoder (3rd row), the similarity of the main reconstructive area is better than only using image vector-pairs, (x , x') (the 2nd row). Then, we add the AT2 vector-pairs (x_2 , x'_2), and the reconstructed similarity is improved, especially on the key image regions (bottom row). Changes occur when gradually adding the attention regions, as shown in Fig. 10. Training one attention region benefits the similarities of corresponding regions, and the attention regions contribute a higher fidelity to the reconstructed face.

Next, we compare the center-aligned TSA to the misaligned (Gram-CAM-based) TSA. We select the LSUN cats 256×256 dataset on StyleGANv2. The target (cat) positions in the image are random so that the dataset contains misaligned images. As shown in Fig. 11, for the encoder case 1, the Grad-CAM-based TSA is better than the center-aligned TSA (rows 2 and 3). For case 2, the training tasks easily fail. We remove the z_c gradients to decrease the training obstacles, but the center-aligned TSA still failed. It is noted that reconstructions via center-aligned TSA cannot synthesize cat eyes (4th row). The Gram-CAM-based TSA could work well on case 2 but with some blurring.

D. Real Image Process

As shown in Fig. 12, real images can be processed by directly using learned attribute directions based on the MTV-TSA reconstruction [30]. Using StyleGANv1, we set the embedded style vectors as w , the attribute direction as d , and the coefficient of d as α . Finally, the changed latent style vectors are denoted as $w' = w + \alpha \cdot d$. We find that as more layers of w are changed, the more obvious the transformation is in the semantic attribute; however, the face identity can also be changed. Thus, only partial style layers need to be used to

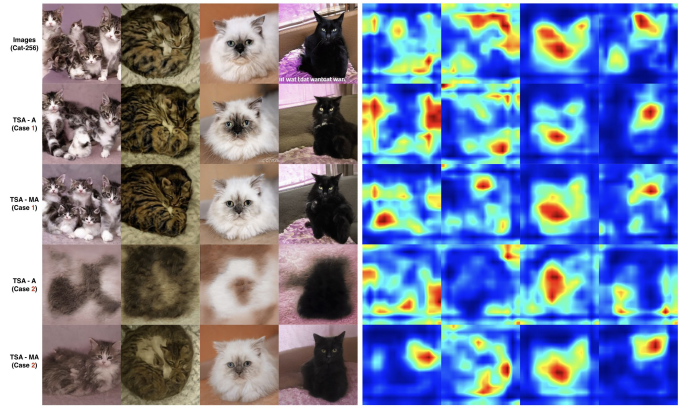


Fig. 11. The 1st row shows generated images from StyleGANv2 (dataset of LSUN 256×256 cats). Based on the MTA-TSA, the 2nd and 3rd rows show the case 1 reconstructed results; the 2nd row shows the center-aligned TSA, and the 3rd row shows Grad-CAM-based TSA. The 4th and 5th rows show the case 2 reconstructed results; the 4th row comes from the center-aligned TSA, and the 5th row comes from the Gram-CAM-based TSA.



Fig. 12. Real image processing using the MTA-TSA on StyleGANv1 FFHQ. Two learning directions (smile and pose) are taken directly from a supervised training method via attribute classification (SVM) [30]. Both directions are added in the first 4 block style vectors w .

achieve the ideal attribute transformation. Here, we choose w from the first 4 layers and suitable values for α and its d .

VI. CONCLUSION

To handle HQ image embedding and reconstruction, we revisit and analyze the relationships between latent space and images in GANs, especially in StyleGANs. We propose the MTV-TSA as a GAN-based method to embed images to latent space via encoders. In latent space, we propose the MTV to support better latent representation for images. On HQ images, we offer the TSA to improve the reconstruction similarity. For aligned images, the center-aligned TSA emphasizes the outstanding regions. The Grad-Cam-based TSA solved misaligned images in which prominent targets appeared in random areas. The MTV-TSA could be implemented on recent famous GANs (PGGAN, StyleGANs, and BigGAN). Based on the pre-trained encoder from the MTV-TSA, real images were better embedded into latent space. Moreover, driving the latent vectors via learned attribute directions allow processing real

images, such as human faces. Learning attribute directions based on latent vectors is a valuable exploration in the future.

REFERENCES

- [1] T. Karras, S. Laine, and T. Aila, "A style-based generator architecture for generative adversarial networks," in *Proc. IEEE Conf. Comput. Vis. Pattern Recognit (CVPR)*, June 2019.
- [2] I. Goodfellow, J. Pouget-Abadie, M. Mirza, B. Xu, D. Warde-Farley, S. Ozair, A. Courville, and Y. Bengio, "Generative adversarial nets," in *Proc. Adv. Neural Inf. Process. Syst. (NIPS)*, vol. 27, 2014, pp. 2672–2680.
- [3] A. Radford, L. Metz, and S. Chintala, "Unsupervised representation learning with deep convolutional generative adversarial networks," in *Int. Conf. Learn. Representations (ICLR)*, 2016.
- [4] T. Karras, T. Aila, S. Laine, and J. Lehtinen, "Progressive growing of gans for improved quality, stability, and variation," in *Int. Conf. Learn. Representations (ICLR)*, 2018.
- [5] A. Brock, J. Donahue, and K. Simonyan, "Large scale GAN training for high fidelity natural image synthesis," in *Int. Conf. Learn. Representations (ICLR)*, 2019.
- [6] A. Karnewar and O. Wang, "Msg-gan: Multi-scale gradients for generative adversarial networks," in *Proc. IEEE Conf. Comput. Vis. Pattern Recognit (CVPR)*, June 2020.
- [7] T. Miyato, T. Kataoka, M. Koyama, and Y. Yoshida, "Spectral normalization for generative adversarial networks," in *Int. Conf. Learn. Representations (ICLR)*, 2018.
- [8] I. Gulrajani, F. Ahmed, M. Arjovsky, V. Dumoulin, and A. C. Courville, "Improved training of wasserstein gans," in *Proc. Adv. Neural Inf. Process. Syst. (NIPS)*, 2017, pp. 5767–5777.
- [9] T. Salimans, I. J. Goodfellow, W. Zaremba, V. Cheung, A. Radford, and X. Chen, "Improved techniques for training gans," in *Proc. Adv. Neural Inf. Process. Syst. (NIPS)*, 2016, pp. 2226–2234.
- [10] K. He, X. Zhang, S. Ren, and J. Sun, "Deep residual learning for image recognition," in *Proc. IEEE Conf. Comput. Vis. Pattern Recognit (CVPR)*, 2016, pp. 770–778.
- [11] T. Karras, S. Laine, M. Aittala, J. Hellsten, J. Lehtinen, and T. Aila, "Analyzing and improving the image quality of stylegan," in *Proc. IEEE Conf. Comput. Vis. Pattern Recognit (CVPR)*, 2020, pp. 8107–8116.
- [12] M. Mirza and S. Osindero, "Conditional generative adversarial nets," vol. abs/1411.1784, 2014.
- [13] W. Xia, Y. Zhang, Y. Yang, J. Xue, B. Zhou, and M. Yang, "GAN inversion: A survey," *arXiv preprint*, vol. abs/2101.05278, 2021.
- [14] J. Donahue, P. Krähenbühl, and T. Darrell, "Adversarial feature learning," in *Int. Conf. Learn. Representations (ICLR)*, 2017.
- [15] A. Creswell and A. A. Bharath, "Inverting the generator of a generative adversarial network," *IEEE Trans. Neural Networks Learn. Syst.*, vol. 30, no. 7, pp. 1967–1974, 2019.
- [16] R. Abdal, Y. Qin, and P. Wonka, "Image2stylegan: How to embed images into the stylegan latent space?" in *Proc. IEEE Int. Conf. Comput. Vis. (ICCV)*, 2019, pp. 4431–4440.
- [17] J. Zhu, Y. Shen, D. li Zhao, and B. Zhou, "In-domain gan inversion for real image editing," in *Proc. Eur. Conf. Comput. Vis. (ECCV)*, 2020.
- [18] S. Pidhorskyi, D. A. Adjeroh, and G. Doretto, "Adversarial latent autoencoders," in *Proc. IEEE Conf. Comput. Vis. Pattern Recognit (CVPR)*, 2020.
- [19] E. Richardson, Y. Alaluf, O. Patashnik, Y. Nitzan, Y. Azar, S. Shapiro, and D. Cohen-Or, "Encoding in style: a stylegan encoder for image-to-image translation," in *Proc. IEEE Conf. Comput. Vis. Pattern Recognit (CVPR)*, June 2021.
- [20] J. Donahue and K. Simonyan, "Large scale adversarial representation learning," in *Proc. Adv. Neural Inf. Process. Syst. (NIPS)*, 2019, pp. 10 541–10 551.
- [21] R. Zhang, P. Isola, A. A. Efros, E. Shechtman, and O. Wang, "The unreasonable effectiveness of deep features as a perceptual metric," in *Proc. IEEE Conf. Comput. Vis. Pattern Recognit (CVPR)*, 2018.
- [22] A. Horé and D. Ziou, "Image quality metrics: Psnr vs. ssim," in *Proc. Int. Conf. Pattern Recognit. (ICPR)*, Istanbul, Aug 2010, pp. 2366–2369.
- [23] Zhou Wang, A. C. Bovik, H. R. Sheikh, and E. P. Simoncelli, "Image quality assessment: from error visibility to structural similarity," *IEEE Trans. Image Process.*, vol. 13, no. 4, pp. 600–612, 2004.
- [24] D. Brunet, E. R. Vrscay, and Z. Wang, "On the mathematical properties of the structural similarity index," *IEEE Trans. Image Process.*, vol. 21, no. 4, pp. 1488–1499, 2012.
- [25] Z. Wang and Q. Li, "Information content weighting for perceptual image quality assessment," *IEEE Trans. Image Process.*, vol. 20, no. 5, pp. 1185–1198, 2011.
- [26] M. P. Sampat, Z. Wang, S. Gupta, A. C. Bovik, and M. K. Markey, "Complex wavelet structural similarity: A new image similarity index," *IEEE Trans. Image Process.*, vol. 18, no. 11, pp. 2385–2401, 2009.
- [27] A. Rehman and Z. Wang, "Reduced-reference image quality assessment by structural similarity estimation," *IEEE Trans. Image Process.*, vol. 21, no. 8, pp. 3378–3389, 2012.
- [28] S. Wang, A. Rehman, Z. Wang, S. Ma, and W. Gao, "Perceptual video coding based on ssim-inspired divisive normalization," *IEEE Trans. Image Process.*, vol. 22, no. 4, pp. 1418–1429, 2013.
- [29] Z. Wang, A. Bovik, H. Sheikh, and E. Simoncelli, "Image quality assessment: from error visibility to structural similarity," *IEEE Trans. Image Process.*, vol. 13, no. 4, pp. 600–612, 2004.
- [30] Y. Shen, C. Yang, X. Tang, and B. Zhou, "Interfacegan: Interpreting the disentangled face representation learned by gans," *IEEE Trans. Pattern Anal. Mach. Intell.*, 2020.
- [31] Y. Choi, M. Choi, M. Kim, J. Ha, S. Kim, and J. Choo, "Stargan: Unified generative adversarial networks for multi-domain image-to-image translation," in *Proc. IEEE Conf. Comput. Vis. Pattern Recognit (CVPR)*, 2018, pp. 8789–8797.
- [32] Y. Choi, Y. Uh, J. Yoo, and J. Ha, "Stargan v2: Diverse image synthesis for multiple domains," in *Proc. IEEE Conf. Comput. Vis. Pattern Recognit (CVPR)*, 2020, pp. 8185–8194.
- [33] Z. He, W. Zuo, M. Kan, S. Shan, and X. Chen, "Attgan: Facial attribute editing by only changing what you want," *IEEE Trans. Image Process.*, vol. 28, no. 11, pp. 5464–5478, 2019.
- [34] D. P. Kingma and M. Welling, "Auto-encoding variational bayes," in *Int. Conf. Learn. Representations (ICLR)*, 2014.
- [35] T. White, "Sampling generative networks," in *Proc. Adv. Neural Inf. Process. Syst. (NIPS)*, 2016.
- [36] J. Zhu, P. Kr, E. Shechtman, and A. A. Efros, "Generative visual manipulation on the natural image manifold," in *Proc. Eur. Conf. Comput. Vis. (ECCV)*, 2016, pp. 597–613.
- [37] E. Härkönen, A. Hertzmann, J. Lehtinen, and S. Paris, "Ganspace: Discovering interpretable GAN controls," in *Advances in Neural Information Processing Systems 33: Annual Conference on Neural Information Processing Systems 2020, NeurIPS 2020, December 6–12, 2020, virtual*, H. Larochelle, M. Ranzato, R. Hadsell, M. Balcan, and H. Lin, Eds., 2020.
- [38] K. Simonyan and A. Zisserman, "Very deep convolutional networks for large-scale image recognition," in *Int. Conf. Learn. Representations (ICLR)*, Y. Bengio and Y. LeCun, Eds., 2015.
- [39] A. Krizhevsky, I. Sutskever, and G. E. Hinton, "Imagenet classification with deep convolutional neural networks," *Commun. ACM*, vol. 60, no. 6, pp. 84–90, 2017.
- [40] J. Deng, W. Dong, R. Socher, L. Li, K. Li, and F. Li, "Imagenet: A large-scale hierarchical image database," in *Proc. IEEE Conf. Comput. Vis. Pattern Recognit (CVPR)*, 2009, pp. 248–255.
- [41] B. Zhou, A. Khosla, À. Lapedriza, A. Oliva, and A. Torralba, "Learning deep features for discriminative localization," in *Proc. IEEE Conf. Comput. Vis. Pattern Recognit (CVPR)*, 2016, pp. 2921–2929.
- [42] R. R. Selvaraju, M. Cogswell, A. Das, R. Vedantam, D. Parikh, and D. Batra, "Grad-cam: Visual explanations from deep networks via gradient-based localization," *Int. J. Comput. Vis.*, vol. 128, no. 2, pp. 336–359, 2020.
- [43] C.-H. Lee, Z. Liu, L. Wu, and P. Luo, "Maskgan: Towards diverse and interactive facial image manipulation," in *Proc. IEEE Conf. Comput. Vis. Pattern Recognit (CVPR)*, 2020, pp. 5549–5558.
- [44] X. Glorot and Y. Bengio, "Understanding the difficulty of training deep feedforward neural networks," in *Proc. Int. Conf. AI. and Stats. (AISTATS)*, Y. W. Teh and D. M. Titterton, Eds.
- [45] D. Ulyanov, A. Vedaldi, and V. S. Lempitsky, "Instance normalization: The missing ingredient for fast stylization," *arXiv preprint*, vol. abs/1607.08022, 2016.
- [46] F. Yu, Y. Zhang, S. Song, A. Seff, and J. Xiao, "Lsun: Construction of a large-scale image dataset using deep learning with humans in the loop," *arXiv preprint*, vol. abs:1506.03365.
- [47] D. P. Kingma and J. Ba, "Adam: A method for stochastic optimization," in *Int. Conf. Learn. Representations (ICLR)*, Y. Bengio and Y. LeCun, Eds., 2015.

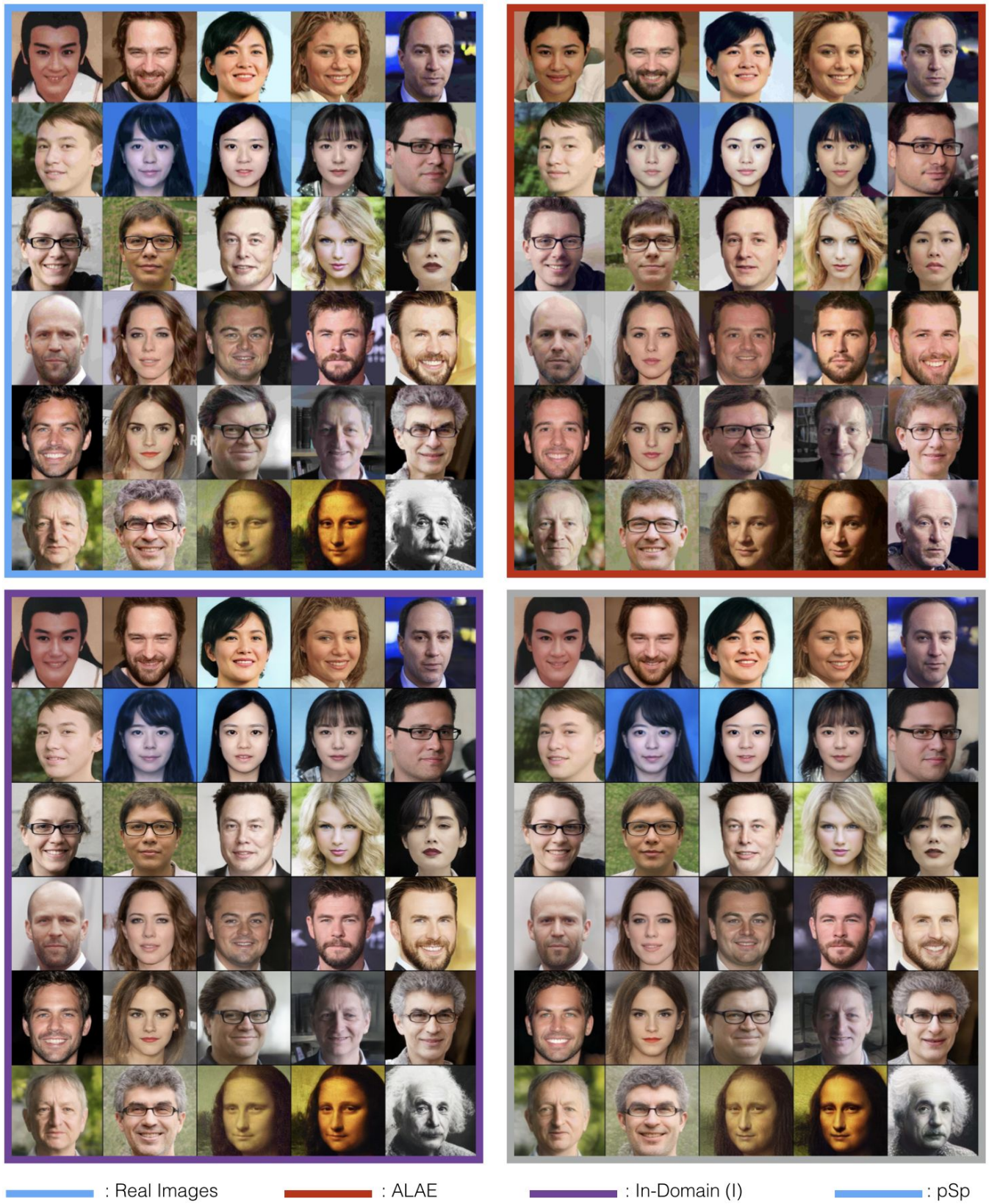


Fig. 13. Reconstruction results with real images. From left to right are real images and the reconstructed images from ALAE, In-Domain(I), and pSp.



Fig. 14. Reconstruction results from the MTV-TSA. The reconstructions are taken from E which is further optimized 1,500 times.